Revision 2

1   **Spin transition of Fe^{2+} in Earth's transition-zone ringwoodite $(Mg,Fe)_2SiO_4$ at high pressures**

2

3   Igor S. Lyubutin[1], Jung-Fu Lin[2], Alexander G. Gavriliuk[1,3], Anna A. Mironovich[3],

4   Anna G. Ivanova[1], Vladimir V. Roddatis[4], and Alexander L. Vasiliev[1,4]

5   *[1]Shubnikov Institute of Crystallography, Russian Academy of Sciences, Moscow 119333, Russia*

6   *[2]Department of Geological Sciences, Jackson School of Geosciences, The University of Texas at*

7   *Austin, Austin, Texas 78712-0254*

8   *[3] Institute for Nuclear Research, Russian Academy of Sciences, 60-letiya Oktyabrya prospekt 7a,*

9   *Moscow 117312, Russia*

10   *[4] National Scientific Center, "Kurchatov Institute," Moscow 123098, Russia*

11   **Abstract**

12   Electronic spin transitions of iron in the Earth's mantle minerals are of great interest to

13   deep-Earth researchers because their effects on the physical and chemical properties of mantle

14   minerals can significantly affect our understanding of the properties of the deep planet. Here we

15   have studied the electronic spin states of iron in ringwoodite $(Mg_{0.75}Fe_{0.25})_2SiO_4$ using synchrotron

16   Mössbauer spectroscopy in a diamond anvil cell up to 82 GPa. The starting samples were analyzed

17   extensively using transmission and scanning electron microscopes to investigate nano-scale crystal

18   chemistry and local iron distributions. Analyses of the synchrotron Mössbauer spectra at ambient

19   conditions reveal two non-equivalent iron species, $(Fe^{2+})_1$ and $(Fe^{2+})_2$, which can be attributed to

20   octahedral and tetrahedral sites in the cubic spinel structure, respectively. High-pressure Mössbauer

21   measurements show the disappearance of the hyperfine quadrupole splitting (QS) of the Fe^{2+} ions in

22   both sites at approximately 45-70 GPa, indicating an electronic high-spin (HS) to low-spin (LS)

23   transition. The spin transition exhibits a continuous crossover nature over a pressure interval of

24   approximately 25 GPa, and is reversible in decompression. Our results here provide the first

25   experimental evidence for the occurrence of the spin transition in the spinel-structured ringwoodite,

26   a mantle olivine polymorph, at high pressures.

27   **Keywords:** ringwoodite $(Mg,Fe)_2SiO_4$, high pressure, spin crossover, Mössbauer spectroscopy

Revision 2

Introduction

Earth's transition zone is mainly composed of Fe-bearing Mg_2SiO_4 polymorphs. Extensive studies have been devoted to studying their structural stability as well as their physical and chemical properties under relevant pressure-temperature (P-T) conditions of the region (e.g., Akimoto and Ida 1966; Ringwood and Major, 1966; Suito 1972; Ohtani 1974; Yagi et al. 1974; Morishima et al.1994; Fei and Bertka 1999; Koch-Müller et al. 2009). Three polymorphs of Fe-bearing Mg_2SiO_4 are widely considered to be potentially present in the upper mantle: (1) olivine $[\alpha\text{-}(Mg,Fe)_2SiO_4]$, which occurs abundantly in upper-mantle peridotite; (2) wadsleyite $[\beta\text{-}(Mg,Fe)_2SiO_4]$ with the modified spinel (SPL) structure, which occurs at pressures (P) exceeding 13 GPa and temperature of above approximately 1000°C; (3) ringwoodite $[\gamma\text{-}(Mg,Fe)_2SiO_4]$ with the spinel structure (SP), which exists at P-T conditions between approximately 520 km (P~ 17.5 GPa, T~2000K) and 670 km (P~24 GPa, T~2200K) in depth. These studies have also shown that wadsleyite is not stable in the Fe_2SiO_4–rich portion of the system in which fayalite ($\alpha\text{-}Fe_2SiO_4$) transforms directly into $\gamma\text{-}Fe_2SiO_4$ (SP) at approximately 5.3 GPa and 1000°C (Frost, 2008). On the other hand, Wooland and Angel (1998) have synthesized a phase isostructural to wadsleyite containing a significant amount of Fe^{3+}. Their synthesis was performed using a mixture of fayalite and magnetite at 5.6 GPa and 1100°C. Wooland and Angel (2002) further showed that the Fe_2SiO_4 - Fe_3O_4 series consists of three spinel-like polytypes isostructural to modified spinel phases II, III, and V in Ni-Al silicate systems. Koch et al. (2004) added Mg_2SiO_4 into the Fe_2SiO_4 - Fe_3O_4 series and subjected the mixture to between 4 and 9 GPa and 1100°C, producing three intermediate phases of the modified spinel II, III, and V. They showed that the maximum Mg content in the phase III is limited to 15 mol.% Mg_2SiO_4. These previous studies thus indicate very rich crystal chemistry in the Fe_2SiO_4 - Mg_2SiO_4 series as a function of P-T and iron content.

Understanding the physics and chemistry of these polymorphs as a function of P-T and iron content is of great interest to deep-Earth researchers because such information may help us decipher geophysical and geochemical processes in the Earth's mantle. These reported structural

2

Revision 2

54   modifications are based on the cubic close-packed oxygen sublattices that differ in the packing of

55   the structural units represented by one tetrahedron and two octahedra. In these structural

56   modifications, the tetrahedrally-coordinated Si^{4+} ion is partially replaced by Fe^{3+} ion in all these

57   polymorphs while Fe^{2+} is partially replaced by Fe^{3+} in order to retain the charge balance. Yamanaka

58   et al. (1998, 2001) and van Aken and Woodland (2006) also observed a disordering of Si^{4+} between

59   tetrahedral and octahedral sites of the modified spinel V phase, in which 7% of the Si^{4+} was found

60   to be in the octahedral site. This type of cation disorder in ferromagnesian silicate spinel has been

61   discussed and reviewed in details by Hazen et al. (1993a, 1993b, 1999).

62   Pressure-induced electronic spin-pairing transitions of iron and their associated effects on

63   the physical properties of host phases have been recently observed to occur in lower-mantle

64   minerals including ferropericlase, silicate perovskite, and post-perovskite at high P-T (e.g., see Lin

65   and Tsuchiya (2008) for a review). Specifically, the spin crossover of Fe^{2+} in ferropericlase occurs

66   over a wide P-T range extending from the middle to the lower section of the lower mantle (Lin et al.

67   2007; Lyubutin et al. 2009; Mao et al. 2011). Iron is the most abundant $3d$ transition metal in the

68   Earth's interior; its existence in mantle minerals has been documented to affect a broad spectrum of

69   the minerals' physical and chemical properties (e.g., McCammon 1997, 2006; Irifune et al. 2010).

70   In particular, changes in the spin and valence states of iron as a function of P-T have attracted great

71   interest because they can affect physical, chemical, rheological, and transport properties of the

72   lower-mantle minerals (Lyubutin et al. 2011). Previous studies have focused mainly on the spin and

73   valence states of the lower-mantle minerals, whereas our knowledge on the spin and valence states

74   of iron in transition zone minerals, such as ringwoodite, is largely lacking.

75   Here we have studied the spin and valence states of iron in transition-zone ringwoodite

76   using synchrotron Mössbauer spectroscopy (SMS) in a diamond anvil cell (DAC). Due to the

77   complex crystal chemistry of the olivine polymorphs reported previously and mentioned above, we

78   have used a number of advanced analytical techniques to characterize the starting sample, including

79   energy dispersive X-ray microanalysis (EDXMA), transmission/scanning electron microscopy

3

80   (TEM/STEM), and electron diffraction (ED) to help interpret high-pressure Mössbauer results. Our

81   results here are applied to further understand the nature of the spin transition in Earth's mantle

82   minerals at high pressures.

83

Experimental methods

Sample Synthesis and Characterization

86   Polycrystalline samples were synthesized in a multi-anvil apparatus using ^{57}Fe-enriched

87   starting material ((Mg,Fe)O-SiO$_2$ mixture) in a Pt capsule at targeted conditions of approximately

88   22 GPa and 2000 K; however, the real sample temperature was likely in the ringwoodite stability

89   field (lower temperature than expected). The synthesized sample was extracted from the capsule

90   and extensively analyzed using EDXMA, TEM, ED, and SMS. For the TEM analyses, several

91   cross-sections of the sample were prepared by Focus Ion Beam(FIB) milling technique using a

92   Helios dual beam system (FEI, Oregon , U.S.A.), which combines Scanning Electron Microscope

93   and FIB (SEM/FIB) equipped with C and Pt gas injectors and micromanipulator (Omniprobe, TX,

94   US). A Pt layer 2-3 μm thick was deposited on the surface of the sample prior to the cross-section

95   preparation by FIB milling procedure. Cross sections measuring with a surface area of 8x5 μm^2 and

96   a thickness of 0.5 μm were cut by 30 kV Ga$^+$ ions, removed from the bulk sample, and then attached

97   to an Omniprobe semi-ring (Omniprobe, TX, US). Final thinning was performed with 30 kV Ga$^+$

98   ions followed by cleaning with 2 keV Ga$^+$ ions to allow for the electron transparency in

99   TEM/STEM experiments. All specimens were studied using a transmission/scanning electron

100   microscope Titan 80-300 (FEI, Oregon, US) equipped with a spherical aberration (C$_s$) corrector

101   (electron probe corrector), a high angle annular dark field (HAADF) detector, an atmospheric thin-

102   window energy dispersive X-ray (EDX) spectrometer (Phoenix System, EDAX, Mahwah, NJ, US),

103   and post-column Gatan energy filter (GIF; Gatan, Pleasanton, CA, US). The TEM analyses were

104   performed at 300 kV. RAPID CCD camera was used to record electron diffraction patterns. Since

105   high-pressure synthesized samples were likely sensitive to irradiation of the electron beam, we also

4

106   used a liquid nitrogen (LN_2) cooled holder (Gatan 636 Double Tilt, Gatan, PA, US) to prevent

107   potential sample decomposition and/or amorphization during the study (see results for details).

108

109   **High-Pressure Synchrotron Mössbauer Spectroscopic Measurements**

110   Electronic spin and valence states of iron ions in the synthesized sample were studied using

111   SMS technique (also called Nuclear Forward Scattering (NFS)) in a DAC at the 16ID-D sector of

112   the HPCAT Beamline (Sector 16) of the Advanced Photon Source, Argonne National Laboratory

113   (APS, ANL). A double-polished sample platelet with dimensions of approximately 80 x 80 μm^2 in

114   size and 5 μm in thickness was loaded into a DAC having 300 μm diamond-anvil culets. The

115   platelet's effective thickness for the SMS experiments was estimated to be around 2-3 based on

116   fitting results of the Mössbauer spectra (Gavriliuk et al. 2006). A rhenium gasket with an initial

117   thickness of 250 μm was pre-indented to 30 μm and a hole of 150 μm was drilled into the gasket for

118   use as a sample chamber. To maintain quasi-hydrostatic pressure conditions of the sample chamber,

119   mineral oil was loaded into the sample chamber and used as the pressure medium, together with a

120   few ruby chips that acted as pressure calibrants. Pressure in the sample chamber was determined by

121   the ruby fluorescence method (Mao et al. 1978).

122   SMS experiments were performed at 16ID-D beamline of the APS, ANL. A high-resolution

123   monochromator with 2.2 meV bandwidth was tuned to nuclear resonance energy of 14.4125 keV

124   for the Mössbauer transition of ^{57}Fe in the sample (Shvyd'ko et al. 2000). The synchrotron beam

125   was focused down to approximately 60 μm (FWHM) by a pair of KB mirrors and further slit down

126   to about 20 μm using a Pt pinhole of 20 μm in diameter drilled in a 200 μm thick Pt disk. This

127   allowed the SMS spectra to be taken from a relatively small area of the sample with a lesser

128   pressure gradient. Based on the experience learn from our numerous previous experiments, mineral

129   oil serves a quasi-hydrostatic pressure medium with relatively small local stresses in diamond-anvil

130   cell experiments. We also note that we had used several ruby chips across the sample chamber to

131   evaluate pressure gradients from the center to the edge of the chamber. Meanwhile, the SMS spectra

5

Revision 2

132   were collected from a small region of approximately 20 microns near the center of the chamber by

133   using a 20 micron pinhole to define the X-ray beamsize. Based on these analyses, we believed that

134   the pressure gradient across the region of the measured sample was about 2%. These arguments

135   allow us to state that the conditions of measurements were close to hydrostatic. Synchrotron time

136   spectra of the ^{57}Fe nuclei in the sample were recorded by an avalanche photo diode (APD) detector

137   in the forward direction in the pressure range between ambient pressure and 82 GPa during

138   compression and decompression runs. The spectra were evaluated using the MOTIF program

139   (Shvyd'ko 1999) to permit derivation of the hyperfine parameters.

140

141   **Experimental Results**

142   **TEM and STEM Analyses**

143   Low magnification bright field (BF) and HAADF STEM images of the specimen are shown

144   in Figure 1a-d, respectively. In the upper part of the images of sample 1 (Figs. 1a and b), the "hair-

145   like" contrast was a result of the partially-sputtered (by FIB) protective Pt film. These images,

146   together with the image of specimen 2 (Figs. 1c), showed that sample platelet exhibited

147   polycrystalline microstructures consisting of fine grains 0.1 – 1.5 μm in diameter, separated by

148   minor intercalations (ground matrix). Most grains exhibited irregular faceted morphology, though a

149   few grains had rather circular rounded morphology and were surrounded by nano-cracks. These

150   grains were relatively bright in the STEM images (Figs. 1b and c), most likely due to an excess of

151   heavier Fe atoms. Diffraction contrasts of the irregular and rounded particles on the BF TEM

152   images were obtained at higher magnifications (Fig. 1d). The results showed that these grains were

153   single crystals with some internal strain. The minor intercalations, on the other hand, appeared

154   darker in the HAADF STEM images (Figs. 1b and 1c), and could be associated with higher content

155   of light elements including Mg, Si, and O. Energy filtering of the BF images with energy shift 40±5

156   eV, which was chosen experimentally in order to obtain the highest contrast possible, showed that

157   the intercalations were approximately 0.01-0.70 μm thick. The intercalations were made of

6

Revision 2

158   amorphous materials as unambiguously revealed by the analyses of the BF images and further ED

159   studies (Fig. 1d) (see discussion below for details).

160

161   **Energy Dispersive X-ray Microanalysis (EDX Microanalysis)**

162   The results of EDX Fe, Si, and Mg element mapping are presented in Figure 2. These

163   measurements showed that the rounded grains were more Fe-rich while the ground matrix contained

164   more Mg and Si, consistent with the HAADF STEM results. In order to obtain more accurate

165   statistics, we performed semi-quantitative energy dispersive X-ray microanalysis (EDXMA) for a

166   number of grains shown in Figures 1b and 1c. The representative EDXMA spectra are shown in

167   Figure 3. We observed lower than expected O element statistics based on proposed stoichiometry,

168   which may be a result of the presence of the uneven specimen surface and e^- beam induced

169   amorphization, together with low-energy X-ray shielding. On the contrary, excess O content was

170   observed in some areas (see for instance no. 4).

171   The EDXMA data in Figures 1b and 1c and Table 1 indicate that Fe predominantly presents

172   itself in the rounded grains with a chemical formula of $(Mg_{0.75},Fe_{0.25})_2SiO_4$ which is mostly present

173   in the ringwoodite phase (see TEM data below for details), whereas the minor intercalations (a few

174   percent in abundance and mostly less than 1 μm thick) had a stoichiometry very close to $MgSiO_3$

175   with a chemical formula of $(Mg_{0.95},Fe_{0.05})SiO_3$ (as seen, for example, in area no.3 of Fig. 1b).

176   Representative EDXMA spectra obtained from selected areas of two specimens are shown in

177   Figures 3a-c. Since Fe is primarily present in ringwoodite, we conclude that the SMS spectra should

178   not be affected by the presence of minute $(Mg_{0.95},Fe_{0.05})SiO_3$ (see further discussion below).

179

180   **Electron Diffraction (ED) Data**

181   In order to relate the chemical analyses to the crystal structure of the major Fe-rich grains

182   eventually used for Mössbauer measurements, specific grains were further investigated using

183   electron diffraction techniques (Figs. 4a-c). Analyses of the diffraction patterns using inter-planar

7

184   distances and angles between the diffraction maxima indicate that the crystal structure corresponds

185   to a cubic system with a lattice parameter a = 8.06 (±0.10) Å. Moreover, when tilted along the $00l$

186   Kikuchi band to a position between zone axes, a clear modulation of the reflection patterns

187   appeared while odd reflections disappeared (Fig. 4b). We thus conclude that most of the observed

188   reflections at the zone axis orientations must arise from plural scattering, *i.e., 00l* reflections with

189    $l \neq 2n$ may also be kinematically forbidden. The additional row of the reflections from which the

190   multiple scattering occurred was also visible in the selected area electron diffraction (SAED)

191   pattern. Additional evidence for the space group of the $(Mg_{0.75},Fe_{0.25})_2SiO_4$ phase was obtained by

192   tilting the crystal around the $[1\bar{1}1]$ and $[\bar{1}11]$ axes, in which significant decrease in the intensity of

193   the *222* reflections was observed (Fig. 4c). However, we cannot completely rule out the double

194   diffraction effect due to the small distance between the zone axes in reciprocal space.

195   The systematic absences of reflections are what one would expect for the space group

196    $Fd\bar{3}m$ (Hahn 2006). Further verification of this space group and lattice parameters was performed

197   for another zone axis. The SAED pattern corresponding to the B=[310] zone axis (Fig. 5a) together

198   with the respective Kössel ED pattern in the convergent electron beam were also obtained (Fig. 5b).

199   Converting the radius of the first-order Laue zone (FOLZ) ring to a Laue zone spacing parallel to

200   the beam direction, we obtained an inter-planar spacing typical for the structure with the space

201   group $Fd\bar{3}m$ having a lattice parameter of 8.06 (±0.10) Å. Based on all of our detailed chemical

202   and structural analyses of the rounded grains, we conclude that the synthesized sample was mainly

203   made of Fe-rich ringwoodite $((Mg_{0.75},Fe_{0.25})_2SiO_4)$.

204   Analyses of the ED data obtained from the minor intercalations with approximately

205    $(Mg_{0.95},Fe_{0.05})SiO_3$ (area no. 2 in Figure 1b) revealed an orthorhombic crystal structure with the

206   space group *Pnma* and the unit cell parameters a = 4.93 (±0.10) Å, b = 6.90 (±0.10) Å, and c = 4.78

207   (±0.10) Å (O'Keeffe 1979), consistent with the structure of the lower-mantle silicate perovskite. A

208   representative SAED pattern obtained for B= [121] zone axis is presented in Figure 6. Possible

209   existence of other phases with different crystal structures, including enstatite (space group *Pbcn*)

210   (Sasaki et al. 1982), clinoenstatite (space group $P12_1/C1$) (Angel et al.1992), and protoenstatite

211   (space group $Pbcn$) (Murakami et al. 1984), were ruled out based on the analyses of the electron

212   diffraction patterns (Figure 6). These small particles are extremely unstable under the e^- beam

213   irradiation, and can rapidly degrade to an amorphous state, even with the use of a LN_2 cooled

214   sample holder. These observations are consistent with the metastable nature of silicate perovskite at

215   ambient conditions reported previously.

216

High-Pressure Mössbauer Spectroscopy Results

218   Synchrotron ^{57}Fe-Mössbauer spectra of the sample were collected at high pressures up to 82

219   GPa (Figures 7). The starting sample was mostly ringwoodite ($(Mg_{0.75},Fe_{0.25})_2SiO_4$) based on the

220   aforementioned analyses; however, a small amount of perovskite could have been present in the

221   sample. Nevertheless, it should not affect the overall spectra of ringwoodite, as the amount of

222   perovskite and its 1 atomic % iron content are negligible as compared to that of the dominant

223   ringwoodite. In general, the damped decay of nuclear excitation is modulated in time by quantum

224   and dynamic beats (Smirnov 1999). The quantum beats are caused by the interference of the

225   scattered radiation components with different frequencies as a result of the ^{57}Fe nuclear level

226   splitting into sublevels due to the hyperfine interaction. The period of quantum beats is inversely

227   proportional to the hyperfine splitting and, in our case here, to the electric quadrupole splitting

228   (QS). The dynamic beats are caused by multiple scattering processes and are controlled by the

229   sample thickness (Smirnov 1999). The observed low-frequency quantum beats indicate that all iron

230   ions are in a paramagnetic state without magnetic ordering at room temperature.

231   The quantum beats were present in the SMS spectra at pressures up to 45 GPa, underwent

232   significant changes between 35 and 70 GPa, and completely disappeared above 70 GPa. The

233   disappearance of the quadrupole splitting signals an electronic spin transition. The straight-line

234   shape of the nuclear excitation decay observed above 70 GPa indicates an absence of the dynamic

9

235   beats in our thin sample, which simplifies the spectral fitting procedure without the need to consider

236   the dynamic effects on the spectra (Gavriliuk et al. 2006).

237   The Mössbauer spectrum at ambient conditions has a quadrupole doublet shape

238   characteristic of the paramagnetic iron state. The thick sample was analyzed by Mössbauer

239   spectroscopy with a laboratory source at ambient conditions. Analyses of as-measured Mössbauer

240   spectrum showed that 87.8% of the total iron was in the pure Fe^{2+} state (with isomer shift IS = 1.02

241   mm/s) while 12.8% of the iron was in the Fe^{2+}-like state. The value of the isomer shift IS of ~0.69

242   mm/s is close to that of Fe^{2+}, but could also be interpreted as the intermediate state between Fe^{2+}

243   and Fe^{3+} with an averaged valence of $Fe^{2.5+}$. Due to the use of the relatively thick sample,

244   broadening of the spectrum as a result of the thickness effect was quite significant; however, the

245   spectral quality is sufficient enough for us to conclude that the dominant state of the iron ions is

246   Fe^{2+}. Our modeled spectral fitting clearly reveals two intense doublets of the Fe^{+2} ions with the QS

247   values of 2.68 (±0.06) and 1.65 (±0.06) mm/s at ambient conditions. This indicates the presence of

248   two nonequivalent iron sites $(Fe^{2+})_1$ and $(Fe^{2+})_2$ in the ringwoodite structure. We also modeled the

249   spectra with additional considerably weaker doublets, but could not find better reliable fits to the

250   spectra than the two-doublet model. The QS values of the two doublets significantly increase with

251   increasing pressure (Figure 8), and can be represented by linear fits. The calculated parameters for

252    $(Fe^{2+})_1$ and $(Fe^{2+})_2$ sites are: $[QS(P=0)]_1 =2.68\pm0.06$ mm/s, $d(QS)_1/dP=0.0114\pm0.0018$ mm·s^{-1}·GPa^{-1},

253   and $[QS(P=0)]_2 = 1.65 \pm 0.06$ mm/s, $d(QS)_2/dP = 0.0184 \pm0.0016$ mm·s^{-1}·GPa^{-1}.

254   As pressure increases, significant changes in the spectra shape can be seen above 45 GPa

255   (Fig. 7a). Starting from 35 GPa, an additional singlet-line component needs to be added to obtain

256   the best fit to the spectra. The appearance of the singlet-line component reflects the disappearance

257   of the quadrupole splitting of some iron ions, and is indicative of the transition of the high-spin

258   (HS) ions Fe^{2+} with spin $S = 2$ into the low-spin (LS) state with $S = 0$ (Gutlich et al. 2011). With

259   further pressure increase, the intensity of the singlet-line component increases at the expense of the

260   doublet components up to 70 GPa. Above 70 GPa, the singlet-line component is the only remaining

10

261   spectral feature of the Fe^{2+} ions, indicating the completion of the spin-pairing transition in both iron

262   sites. SMS spectra recorded in the pressure release process (Fig. 7b) revealed that the HS-LS

263   transition is reversible (Figs. 7, 8, 9).

264

265   **Discussion**

266   Ringwoodite, a spinel-structured solid solution in the Mg_2SiO_4 - Fe_2SiO_4 series, is a high-

267   pressure polymorph of olivine. As revealed by the electron diffraction patterns, our ringwoodite

268   sample has a lattice parameter a = 8.06 (±0.1) Å in the space group $Fd\bar{3}m$ (Fig. 10). One can thus

269   use Mössbauer spectroscopic analyses to assign iron sites $(Fe^{2+})_1$ and $(Fe^{2+})_2$ in the spinel structure.

270   The QS = 2.68 mm/s of the predominant $(Fe^{2+})_1$ coincides very well with values reported in several

271   previous papers for γ-$(Mg,Fe)_2SiO_4$ ringwoodite (e.g., Choe et al. 1992; O'Neill et al. 1992, 1993;

272   Taran et al. 2009; McCammon et al. 2004; Greenberg et al. 2011), and can be attributed to Fe^{2+}

273   ions in the octahedral site (B-site) of the spinel structure. The $(Fe^{2+})_2$ component with QS = 1.65

274   mm/s can be attributed to Fe^{2+} ions in the tetrahedral sites (A-site) of the structure. In a

275   stoichiometric ringwoodite with a nominal cation distribution $^{VI}[Mg,Fe]_2$ $^{IV}(Si)O_4$, the presence of

276   iron ions in the tetrahedral sites would lead to silicon redistribution from the tetrahedral to

277   octahedral sites, $^{VI}[Mg,Fe,Si]_2$ $^{IV}(Si,Fe)O_4$, producing the inverse or disordered ringwoodite

278   structure. At ambient conditions, this is unlikely from the viewpoint of crystal chemistry due to the

279   large difference in cationic radii between Si^{4+} and Fe^{2+}. However, at high pressures, the spinel

280   structure may be slightly distorted with Si and Fe cations partially occupying both octahedral and

281   tetrahedral sites (Hazen et al. (1993a)). Indeed, Yagi et al. (1974) reported that about 2.3% of the

282   total Si^{4+} cations may occupy the octahedral sites in ringwoodite. This type of cation partial

283   disordering at high P-T in ferromagnesian silicate spinels was discussed and reviewed extensively

284   by Hazen et al. (1993a, 1993b, 1999) and O'Neill et al. (1992). A possible redistribution of Fe^{2+}

285   between octahedral and tetrahedral sites in the inverse ringwoodite structure was also revealed in

286   recent optical absorption spectral measurements (Taran et al. 2009).

11

Revision 2

287   Alternatively, the presence of the two Fe^{2+} doublets in our Mössbauer spectra may arise

288   from differences in the next nearest neighbor environments in the octahedral site of the spinel

289   structure. Both iron species $(Fe^{2+})_1$ and $(Fe^{2+})_2$ may reside in the octahedral site with slightly

290   different local environments. This possibility was previously discussed for the perovskite iron

291   silicates, in which differences in the local environments of the pseudo-dodecahedral site of Fe^{2+}

292   result in doublets with different QS values (e.g., McCammon et al. 1992; Fei et al. 1994;

293   McCammon 1997; Lauterbach et al. 2000). In addition, cation vacancies may appear (ordered or

294   disordered) in the octahedral site of the spinel structure when hydrogen is present in hydrous

295   ringwoodite (e.g., Inoue et al. 1995; Kohlstedt et al.1996; Smyth et al. 2003; McCammon et al.

296   2004). It should also be noted that McCammon et al. (2004) observed a relatively weak Mössbauer

297   absorption in γ-Fe_2SiO_4 ringwoodite with isomer shift $IS = 0.61$ mm/s and $QS = 0.85$ mm/s. They

298   assigned these values to the charge transfer between Fe^{2+} and Fe^{3+} ions in adjacent octahedral sites

299   of the ringwoodite structure.

300   Previous high-pressure Mössbauer measurements on the γ-Fe_2SiO_4 ringwoodite reported a

301   linear decrease of the QS value with increasing pressure up to 16 GPa (Choe et al. 1992). This

302   suggests that no electronic or polymorphic transitions occur up to 16 GPa, except for small and

303   continuous changes of volume and local symmetry under pressure. On the basis of the crystal field

304   calculations, the negative pressure derivative of QS was associated with a trend close to an ideal

305   cubic symmetry of the oxygen sublattice (Choe et al. 1992). A similar decrease of QS was also

306   found in γ-Fe_2SiO_4 at pressures up to 30 GPa (Greenberg et al. 2011).

307   Recent high-pressure X-ray diffraction and Mössbauer spectroscopy measurements on γ-

308   Fe_2SiO_4 (Greenberg et al. 2011) also revealed a structural phase transition to a rhombohedrally-

309   distorted spinel phase at above 30 GPa. Two different Fe^{2+} crystallographic sites with an abundance

310   ratio of $Fe_1:Fe_2 = 3:1$ were observed at pressures above 30 GPa. The ratio correlates with the

311   distorted spinel structure in which Fe_1 is located in a distorted octahedron and Fe_2 is located in a

312   symmetrical octahedron (Greenberg et al. 2011). At pressures above 30 GPa, the QS value in the

313   Fe$_2$ symmetrical site increases, whereas the *QS* value in the Fe$_1$ distorted site continues to decrease.

314   However, no spin transition was observed up to 61 GPa (Greenberg et al. 2011). The high-pressure

315   behavior of the *QS* in our sample is quite different from this previous report, however. With

316   increasing pressure, the *QS* values increase in both iron sites, and the high-spin to low-spin

317   transition clearly occurs in both sites. At room temperature, the spin transition is continuous,

318   reversible, and occurs in the region of 45-70 GPa (Figs. 7 and 8). These differences may be a result

319   of the compositional variation in which Fe-rich γ-Fe$_2$SiO$_4$ helps stabilize the high-spin state.

320   It should be noted that most of the high-pressure Mössbauer measurements were conducted

321   on γ-Fe$_2$SiO$_4$, an end member in the ringwoodite system (Greenberg et al. 2011; Choe et al. 1992),

322   and that the HS-LS spin crossover was not observed at pressures below 61 GPa (Greenberg et al.

323   2011). On the other hand, a spin crossover of Fe^{2+} at pressures between approximately 40 GPa and

324   75 GPa was recently observed in olivine with composition (Mg$_{0.9}$Fe$_{0.1}$)$_2$SiO$_4$ (Rouquette et al.

325   2008). However, the *QS* values are quite different in olivine and ringwoodite. Our findings here

326   indicate that the electronic structures of ringwoodite at high pressures strongly depend on the ratio

327   of Mg and Fe ions in the sample (Mg$_{1-x}$Fe$_x$)$_2$SiO$_4$.

328

329   **Acknowledgments**

341

References cited

343   Akimoto, S. and Ida, Y. (1966) High-pressure synthesis of Mg_2SiO_4. Earth and Planetary Science

344   Letters, 1, 358–359.

345   Angel, R.J., Chopelas, A., and Ross, N.L. (1992) Stability of high-density clinoenstatite at upper-

346   mantle pressures. Nature, 358, 322-324.

347   Choe, I., Ingalls, R., Brown, J.M., and Sato-Sorensen, Y. (1992) Mossbauer Studies of Iron Silicate

348   Spinel at High Pressure. Physics and Chemistry of Minerals, 19, 236-239.

349   Fei, Y. and Bertka, C.M. (1999) Phase transitions in the Earth's mantle and mantle mineralogy. The

350   Geochemical Society Special Publications, 6, 189-207.

351   Fei, Y., Virgo, D., Mysen, B.O., Wang, Y., and Mao, H.K. (1994) Temperature-dependent electron

352   delocalization in $(Mg,Fe)SiO_3$ perovskite. American Mineralogist, 79, 826-837.

353   Frost, D. J. (2008) The upper mantle and transition zone, ELEMENTS, 4 , 171–176

354   Gavriliuk, A.G., Lin, J.F., Lyubutin, I.S., and Struzhkin, V.V. (2006) Optimization of the

355   Synchrotron Mossbauer Experiment for High-Pressure Studies of Electronic Transitions:

356   Magnesiowistite (Mg, Fe)O. JETP Letters, 84, 161–166.

357   Goncharov, A.F., Haugen, B.D., Struzkin, V.V., Beck, P., and Jacobsen, S.D. (2008) Radiative

358   conductivity in the Earth's lower mantle. Nature Letter, 456, 231-234.

359   Greenberg, E., Dubrovinsky, L.S., McCammon, C., Rouquette, J., Kantor, I., Prakapenka, V.,

360   Rozenberg, G.Kh., and Pasternak, M.P. (2011) Pressure-induced structural phase transition of

361   the iron end-member of ringwoodite (γ-Fe_2SiO_4) investigated by X-ray diffraction and

362   Mössbauer spectroscopy. American Mineralogist, 96, 833–840.

363   Gutlich, P., Bill E., and Trautwein, A.X. (2011) Electric Quadrupole Interaction. In Gutlich, P., Bill

364   E., Trautwein, A.X. Eds., Mössbauer spectroscopy and transition metal chemistry, 89-100,

365   Springer-Verlag Berlin Heidelberg.

366   Hahn Th. Ed. (2006) International Tables for Crystallography, vol. A, space-group symmetry, 696–

367   703.

368   Hazen, R.M. (1993a) Comparative crystal chemistry of silicate spinels: Anomalous behavior of

369        $(Mg,Fe)_2SiO_4$. Science, 259, 206-209.

370   Hazen, R.M., Downs, R.T., Finger, L.W., and Ko, J. (1993b) Crystal chemistry of ferromagnesian

371   silicate spinels: evidence for Mg-Si disorder. American Mineralogist, 78, 1320-1323.

372   Hazen, R.M. and Yang, H. (1999) Effect of cation distribution and order disorder on P-V-T

373   equations of states of cubic spinels. American Mineralogist, 84, 1956-1960.

374   Inoue, T., Yurimoto, H., and Kudoh, Y. (1995). Hydrous modified spinel $Mg_{1.75}Si_{0.5}O_4$: a new

375   water reservoir in the mantle transition region. Geophysical Research Letters, 22, 117- 120.

376   Irifune, T., Shinmei, T., McCammon, C.A., Miyajima, N., Rubie, D.C., and Frost, D.J. (2010) Iron

377   partitioning and density changes of pyrolite in Earth's lower mantle. Science, 327, 193-195.

378   Koch, M., Woodland, A.B., and Angel, R.J. (2004) Stability of spinelloid phases in the system

379   Mg_2SiO_4–Fe_2SiO_4–Fe_3O_4 at 1100^0 C and up to 10.5 GPa. Physics of the Earth and Planetary

380   Interiors, 143, 171–183.

381   Koch-Müller, M., Rhede, D., Schulz, R., and Wirth, R. (2009) Breakdown of hydrous ringwoodite

382   to pyroxene and spinelloid at high P and T and oxidizing conditions. Physics and Chemistry of

383   Minerals, 36, 329–341.

384   Kohlstedt, D.L., Keppler, H., and Rubie, D.C. (1996) The solubility of water in α, β and γ phases of

385        $(Mg,Fe)_2SiO_4$. Contributions to Mineralogy and Petrology, 123, 345-357.

386   Lauterbach, S., McCammon, C.A., van Aken, P., Langenhorst, F., and Seifert, F. (2000) Mossbauer

387   and ELNES spectroscopy of $(Mg,Fe)(Si,Al)O_3$ perovskite: a highly oxidised component of the

388   lower mantle. Contributions to Mineralogy and Petrology, 138, 17-26

15

389   Lin, J.F., Vankó, G., Jacobsen, S.D., Iota, V., Struzhkin, V., Prakapenka, V.B., Kuznetsov, A., and

390   Yoo, C.S. (2007a) Spin transition zone in Earth's lower mantle. Science, 317, 1740-1743.

391   Lin, J. F. and Tsuchiya, F. (2008) Spin transition of iron in the Earth's lower mantle. Physics of the

392   Earth and Planetary Interiors, 170, 248-259.

393   Lyubutin, I.S., Gavriliuk A.G., Frolov K.V., Lin J.F., and Trojan I.A. (2009) High-spin-low-spin

394   transition in magnesiowustite $(Mg_{0.75},Fe_{0.25})O$ at high pressures under hydrostatic conditions,

395   JETP Letters, 90, 617-622

396   Lyubutin. I.S., Struzhkin V.V., Mironovich A.A.,. Gavriliuk A.G, Naumov P.G., Lin J.F.,

397   Ovchinnikov S.G., Sinogeikin S., Chow P., and Xiao Y. (2011) Quantum critical point and spin

398   fluctuations in the lower-mantle ferropericlase, Submitted on 18 Oct 2011 to

399   arXiv:1110.3956v1.

400   Mao, H.K., Bell, P.M., Shaner, J.W., and Steinberg, D.J. (1978) Specific volume measurements of

401   Cu, Mo, Pd, and Ag and calibration of the ruby R1 fluorescence pressure gauge from 0.06 to 1

402   Mbar. Journal of Applied Physics, 49, 3276-3283.

403   McCammon, C.A., Rubie, D.C., Ross II, C.R., Seifert, F., and O'Neill, H.S.C. (1992) Mossbauer

404   spectra of $57Fe_{0.05}Mg_{0.95}SiO_3$ perovskite at 80 and 298 K. American Mineralogist, 77, 894-

405   897.

406   McCammon, C. (1997) Perovskite as a possible sink for ferric iron in the lower mantle. Nature,

407   387, 694-696.

408   McCammon, C.A., Frost, D.J., Smyth, J.R., Laustsen, H.M.S., Kawamoto, T., Ross, N.L., and van

409   Akene, P.A. (2004) Oxidation state of iron in hydrous mantle phases: implications for

410   subduction and mantle oxygen fugacity. Physics of the Earth and Planetary Interiors, 143-144,

411   157-169.

412   McCammon, C. (2006) Microscopic properties to macroscopic behavior: the influence of iron

413   electronic states. Journal of Mineralogical and Petrological Sciences 101, 130-144.

414 Mao, Z., Lin, J.F., Liu, J., and Prakapenka V.B. (2011) Thermal equation of state of lower-mantle

415   ferropericlase across the spin crossover. Geophysical Research Letters, 38, L23308.

416 Morishima, H., Kato, T., Suto, M., Ohtani, E., Urakawa, S., Utsumi, W., Shimomura, O., and

417   Kikegawa, T. (1994)The phase boundary between α- and β-Mg2SiO4 determined by in situ X-

418   ray observation. Science, 265, 1202-1203.

419 Murakami, T., Takeuchi, Y., and Yamanaka, T. (1984) X-ray studies on protoenstatite II. Effect of

420   temperature on the structure up to near the incongruent melting point. Zeitschrift fur

421   Kristallographie, 166, 263-275.

422 O'Keeffe, M., Hyde, B.G., and Bovin, J.O. (1979) Contribution to the crystal chemistry of

423   orthorhombic perovskites: $MgSiO_3$ and $NaMgF_3$. Physics and Chemistry of Minerals, 4, 299-

424   305.

425 O'Neill, H.St.C, Annersten, H., and Vargo, D. (1992) The temperature dependence of the cation

426   distribution in magnesioferrite (MgFe2O4) from powder XRD structural refinements and

427   Mössbauer spectroscopy. American Mineralogist, 77, 725-740.

428 O'Neill, H.St.C, McCammon, C.A., Canil, D., Rubie, D.C., Ross II, C.R., and Seifert, H.F. (1993)

429   Mössbauer spectroscopy of mantle transition zone phases and determination of minimum Fe^{3+}

430   content. American Mineralogist, 78, 456-460.

431 Ohtani, E. (1979) Melting relation of Fe_2SiO_4 up to about 200 kbar. Journal of Physics of the Earth,

432   27, 189-208.

433 Ringwood, A.E. and Major, A. (1966) Synthesis of Mg_2SiO_4–Fe_2SiO_4 spinel solid solutions. Earth

434   and Planetary Science Letters, 1, 241-245.

435 Rouquette, J., Kantor, I., McCammon, C.A., Dmitriev, V., and Dubrovinsky, L.S. (2008) High-

436   pressure studies of $(Mg_{0.9},Fe_{0.1})_2SiO_4$ olivine using raman spectroscopy, X-ray diffraction, and

437   Mössbauer spectroscopy. Inorganic Chemistry, 47, 2668–2673.

17

Revision 2

438   Sasaki, S., Takeuchi, Y., Fujino, K., and Akimoto, S. (1982) Electron-density distributions of three

439   orthopyroxenes: $Mg_2Si_2O_6$, $Co_2Si_2O_6$, and $Fe_2Si_2O_6$. Zeitschrift fur Kristallographie, 158, 279-

440   297.

441   Shvyd'ko, Yu.V. (1999) Nuclear resonant forward scattering of x rays: Time and space picture.

442   Physical Review B, 59, 9132-9143.

443   Shvyd'ko, Yu.V., Lerche, M., Jäschke, J., Lucht, M., Gerdau, E., Gerken, M., Rüter, H.D., Wille,

444   H.-C., Becker, P., Alp, E.E., Sturhahn, W., Sutter, J., and Toellneret, T.S. (2000) γ-Ray

445   Wavelength Standard for Atomic Scales. Physical Review Letters, 85, 495-498.

446   Smirnov, G.V. (1999) General properties of nuclear resonant scattering. Hyperfine Interactions,

447   123-124, 31-77.

448   Smyth, J.R., Holl, C.M., Frost, D.J., Jacobsen, S.D., Langenhorst, F., and McCammon, C.A.

449   (2003) Structural Systematics of Hydrous Ringwoodite and Water in Earth's Interior. American

450   Mineralogist, 88, 1402-1407.

451   Suito, K. (1972) Phase transformations of pure Mg_2SiO_4 into a spinel structure under high pressures

452   and temperatures. Journal of Physics of the Earth, 20, 225-243.

453   Suito, K., Tsutsui, Y., Nasu, S., Onodera, A., and Fujita, F.E. (1984) Mossbauer effect study of the

454   γ-form of Fe_2Si0_4. Materials Research Society Symposium Proceedings, 22, p. 295-298

455   Taran, M. N., Koch-Müller, M., Wirth, R., Abs-Wurmbach, I., Rhede, D., and Greshake, A. (2009)

456   Spectroscopic studies of synthetic and natural ringwoodite, gamma-$(Mg, Fe)_2SiO_4$. Physics and

457   Chemistry of Minerals, 36, 217-232.

458   van Aken, P.A. and Woodland, A.B. (2006) Crystal chemistry of spinel and spinelloid solid

459   solutions in the system Fe_2SiO_4–Fe_3O_4. Geophysical Research Abstracts, 8, p. 07770.

460   European Geosciences Union.

461   Woodland, A.B. and Angel, R.J. (1998) Crystal structure of a new spinelloid with the wadsleyite

462   structure in the system Fe_2SiO_4–Fe_3O_4 and implications for the Earth's mantle. American

463   Mineralogist, 83, 404-408.

18

464   Woodland, A.B. and Angel, R.J. (2000) Phase relations in the system fayalite-magnetite at high

465   pressures and temperatures. Contributions to Mineralogy and Petrology, 139, 734-747.

466   Yagi, T., Marumo, F., and Akimoto, S. (1974) Crystal structures of spinel polymorphs of Fe_2SiO_4

467   and Ni_2SiO_4. American Mineralogist, 59, 486-490.

468   Yagi, T., Marumo, F., and Akimoto, S.I. (1974) Crystal structures of spinel polymorphs of Fe_2SiO4

469   and Ni_2SiO_4. American Mineralogist, 59, 486–490.

470   Yamanaka, T., Shimazu, H., and Ota, K. (2001) Electric conductivity of Fe_2SiO_4–Fe_3O_4 spinel solid

471   solutions. Physics and Chemistry of Minerals, 28,110-118.

472   Yamanaka, T., Tobe, H., Shimazu, T., Nakatsuka, A., Dobuchi, Y., Ohtaka, O., Nagai, T., and Ito,

473   E. (1998) Phase relations and physical properties of Fe_2SiO_4–Fe_3O_4 solid solution under

474   pressures up to 12 GPa. In M. Manghnani and T. Yogi, Eds., Properties of earth and planetary

475   materials at high pressure and temperature, p. 457–459. Geophysical Monograph, American

476   Geophysical Union Washington DC.

477

478

19

Revision 2

479   Table 1. Results of the EDX microanalysis (in at.%) in the areas denoted by corresponding

480   numbers in Figure 1b and 1c (accuracy of the measurements is within 1 at.%).

481

482

483

№	Mg	Fe	Si	O	compound
1			33	67	SiO_2
2	21	1	22	56	$(Mg,Fe)SiO_3$
3	20	1	20	59	$(Mg,Fe)SiO_3$
4	4		23	73	$SiO_2 + H_2O$
5	21	6	17	56	$\approx (Mg_{0.78} Fe_{0.22})_2SiO_4$
6	1		39	60	SiO_2
7	21	7	18	53	$\approx (Mg_{0.75} Fe_{0.25})_2SiO_4$
8			50	49	SiO_2
9	16	1	30	52	$(Mg,Fe)Si_2O_3$
10	22	2	24	52	$(Mg,Fe)SiO_3$
11	6		38	55	$MgSiO_x + SiO_2$
12	6		38	55	$MgSiO_x + SiO_2$
13	22	10	18	50	$\approx (Mg_{0.69} Fe_{0.31})_2SiO_4$

484
485
486
487
488
489
490
491
492
493
494
495
496
497
498

499

500

501

502

503

504

505

506

507

508

Revision 2

509   **Figure captions**

510   **Figure 1.** The images of the specimens: (a) The BF TEM image of specimen 1. (b) HAADF STEM

511   image of specimen 1. The areas of EDXMA analyses are indicated. (c) HAADF STEM image of

512   specimen 2 with the indicated areas of EDXMA analyses. (d) Enlarged BF TEM image of

513   ringwoodite particle, the amorphous intercalations are shown by white arrows.

514   **Figure 2.** (a) HAADF STEM image of the specimen and corresponding element distribution

515   mapping results: (b) Fe; (c) Si; (d) Mg.

516   **Figure 3.** Representative EDXMA (energy dispersive X-ray microanalysis) spectra obtained from

517   areas shown in Figures 1b and 1c: (a) area no. 13, similar to the areas no. 5 and no. 7; (b) area no. 3

518   and 10; (c) area no. 6.

519   **Figure 4.** (a) Representative electron-diffraction patterns of ringwoodite ($(Mg,Fe)_2SiO_4$) obtained

520   along B= [110] zone axis. Arrows show the axes around which the sample was rotated to determine

521   the plural scattering effects. (b) The electron diffraction pattern from the sample rotated around the

522   [001] axis. Forbidden reflections are shown by arrows. (c) The electron-diffraction pattern from the

523   sample rotated around the [100] axis. The 222 reflections, demonstrated weak intensities due to the

524   double diffraction (bigger arrows). The reflections responsible for double diffraction are shown by

525   the smaller arrow.

526   **Figure 5**. (a) The SAED pattern obtained in B=[310] zone axis; (b) Respective Kössel electron

527   diffraction pattern demonstrating Kossel-type CBED pattern obtained at the same zone axis

528   orientation as (a). First-order Laue zone ring is shown.

529   **Figure 6.** The SAED pattern from the $MgSiO_3$ grain obtained in B=[121] zone axis.

530   **Figure 7.** SMS spectra of ringwoodite $(Mg_{0.75}Fe_{0.25})_2SiO_4$ at high pressures and room temperature.

531   **Figure 8.** Quadrupole splitting (*QS*) of two iron sites in $(Mg_{0.75}Fe_{0.25})_2SiO_4$ ringwoodite at high

532   pressures and room temperature. Open symbols; compression; solid symbols: decompression.

533   **Figure 9.** High-spin Fe^{2+} abundance as a function of pressure in $(Mg_{0.75}Fe_{0.25})_2SiO_4$ ringwoodite

534   obtained from the SMS spectra at room temperature.

21

Revision 2

535 **Figure 10.** Crystal structure of ringwoodite. Representative Si, Fe, and Mg site occupations are

536 shown to help understand the Mössbauer data interpretation.

537

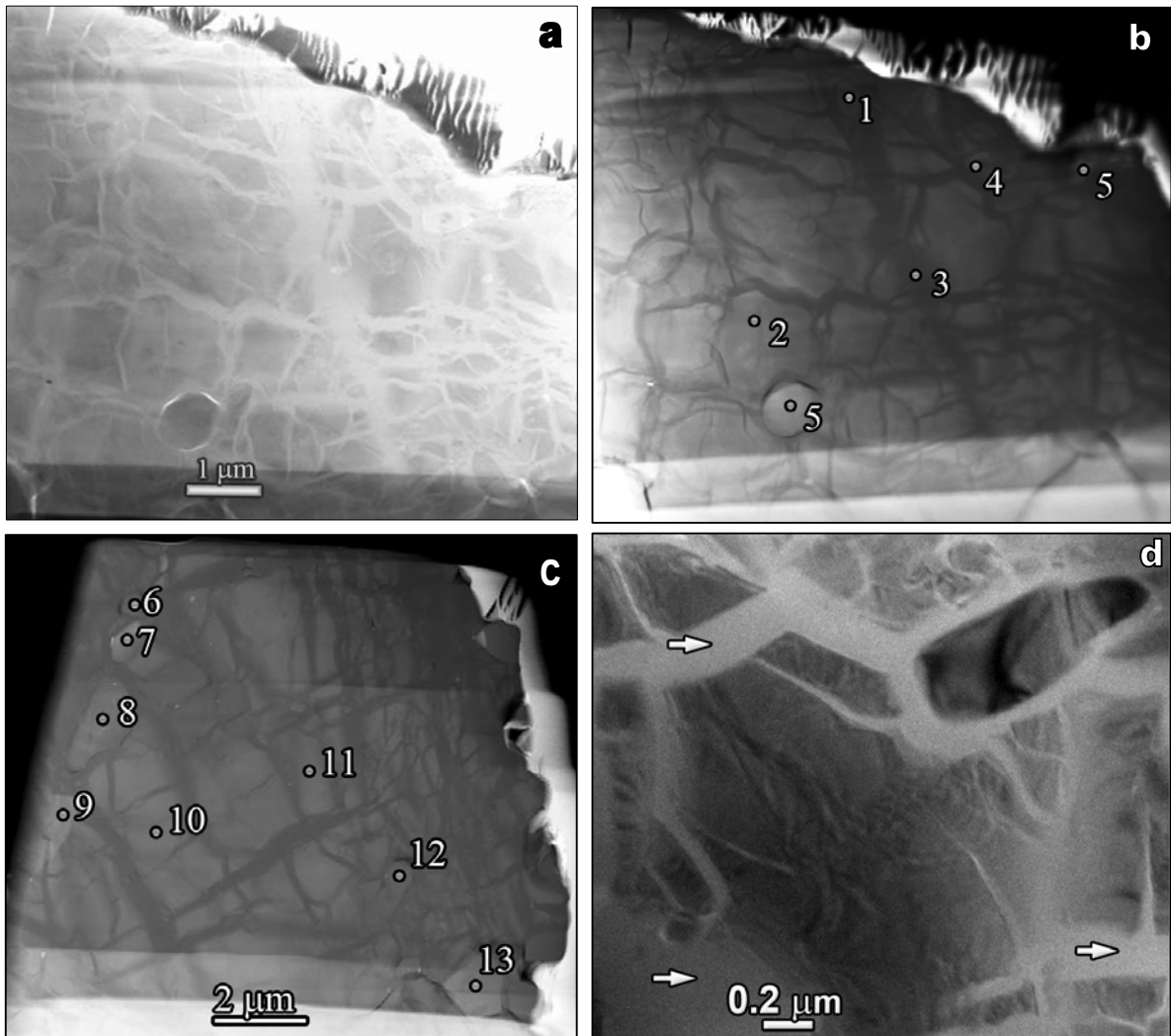Revision 2

538

539

540

541

542

543

544

545

546

547

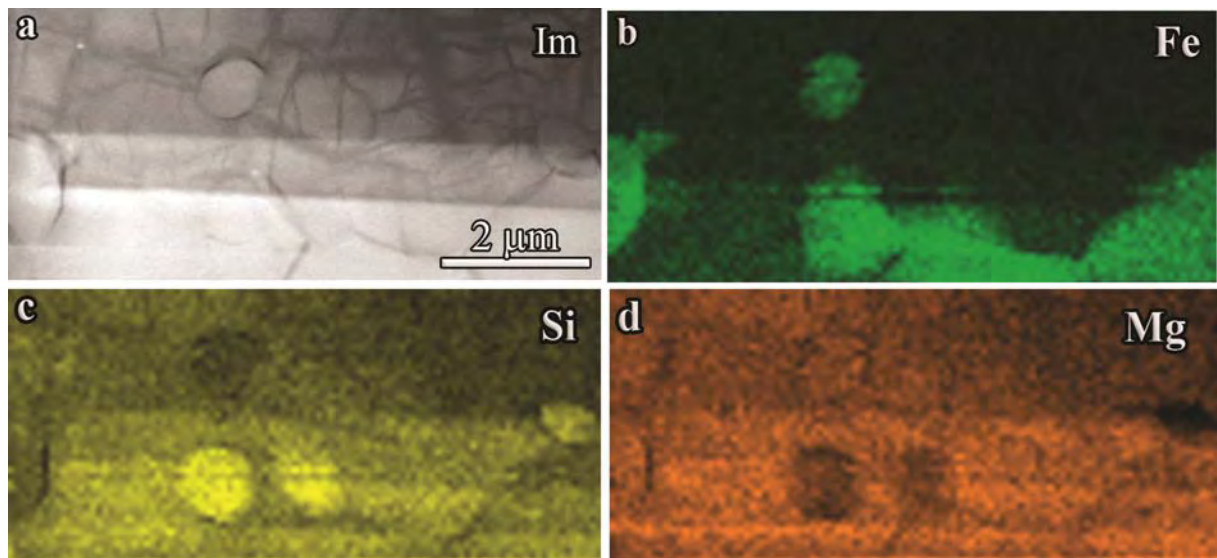548

549

550

551

552

553

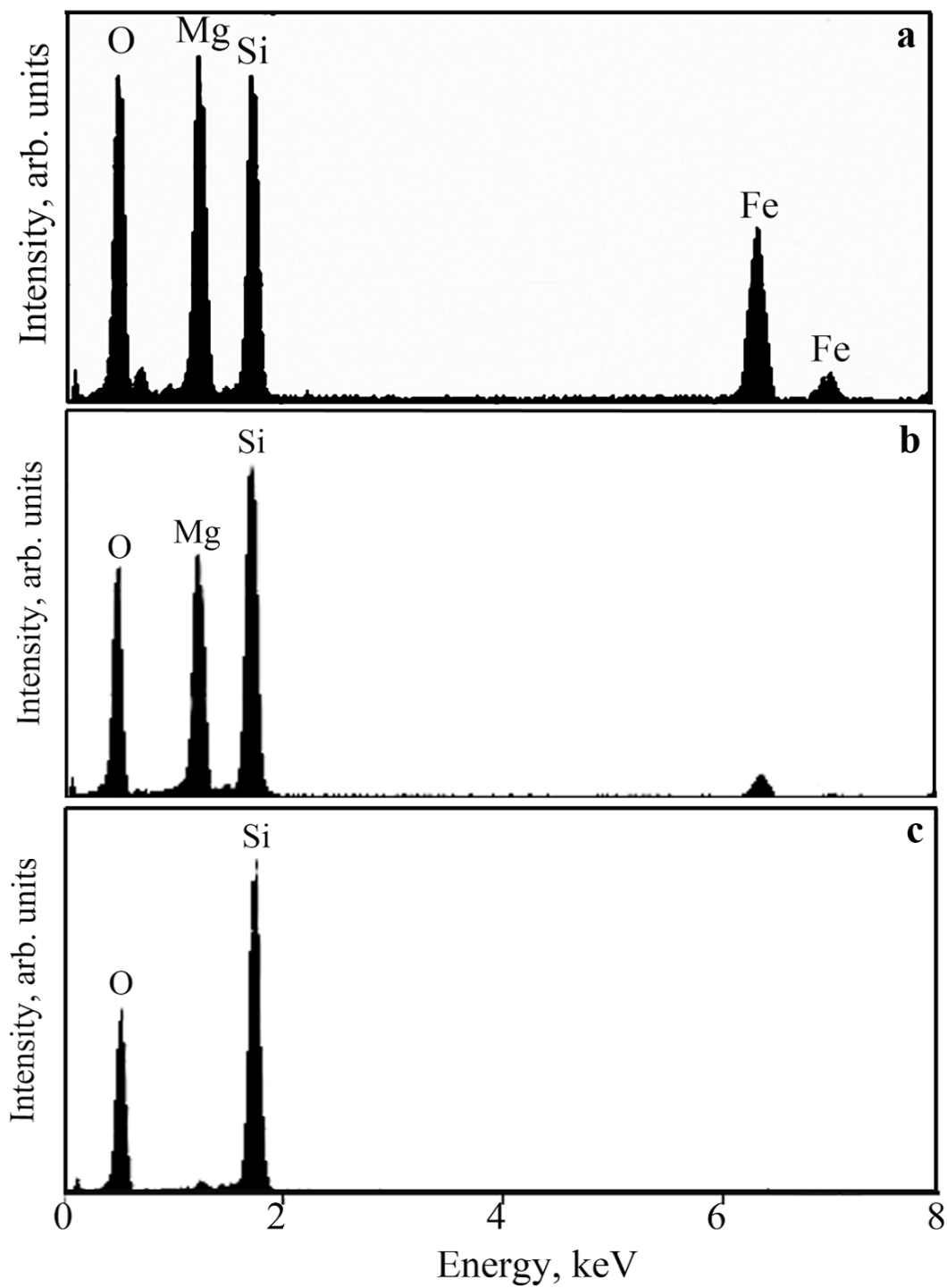554

555

556

557 **Figure 1.**

558

Revision 2

559

560

561   **Figure 2.**

562

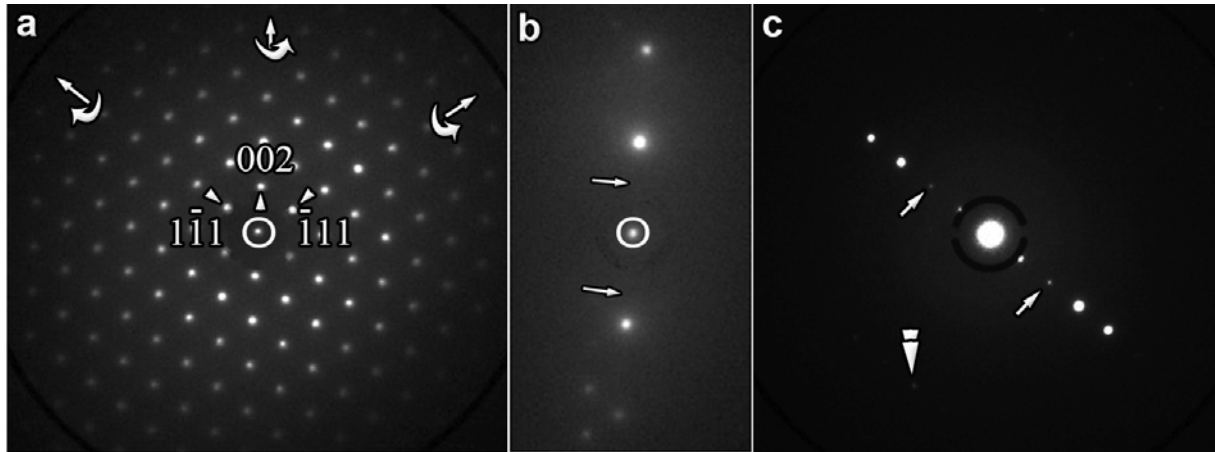563

Revision 2

564

565

566   **Figure 3.**

567

Revision 2

568

569

570

571

572

573

574

575

576

577

578 **Figure 4**

579

Revision 2

580

581

582

583

584
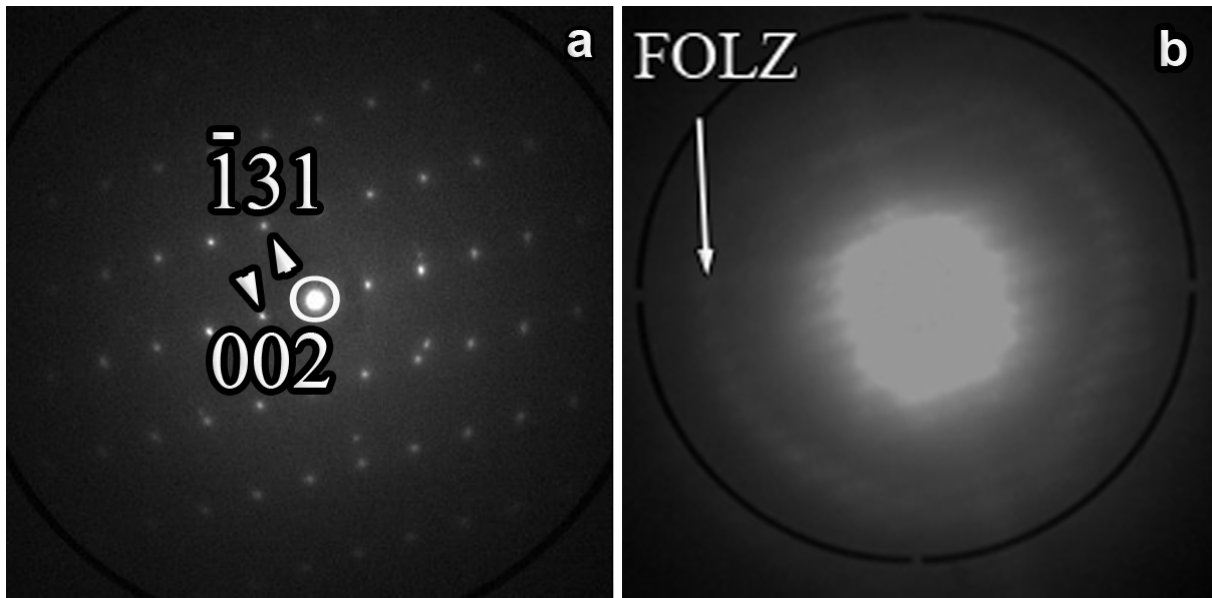
585

586

587

588

589 **Figure 5.**

590

591

Revision 2

592

593

594

595
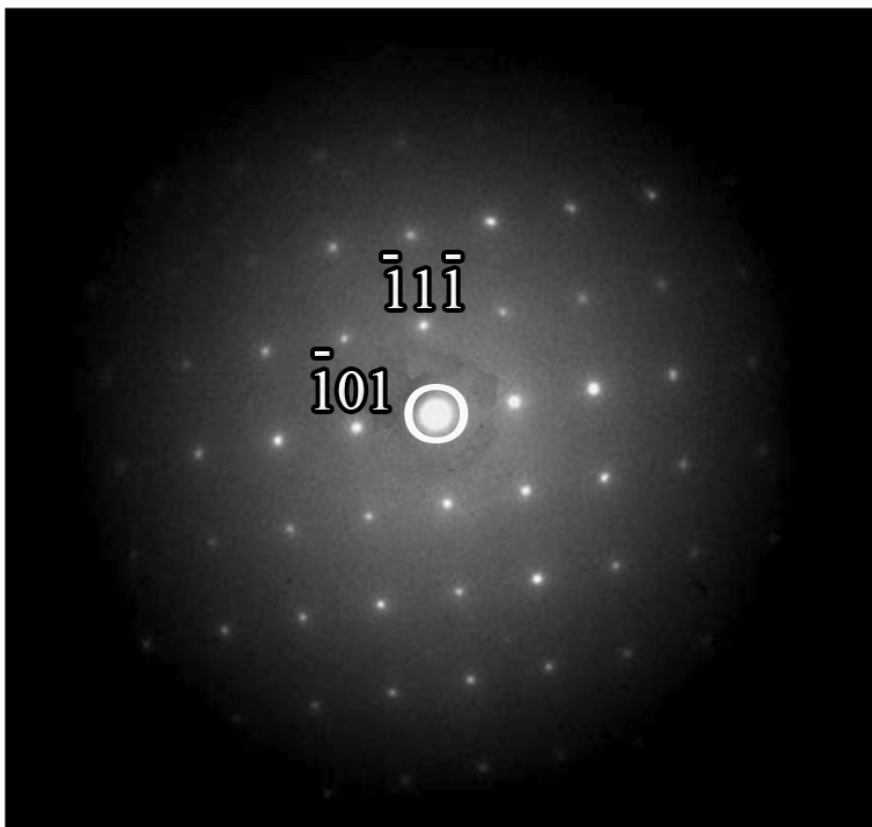
596

597

598

599

600   **Figure 6.**

601

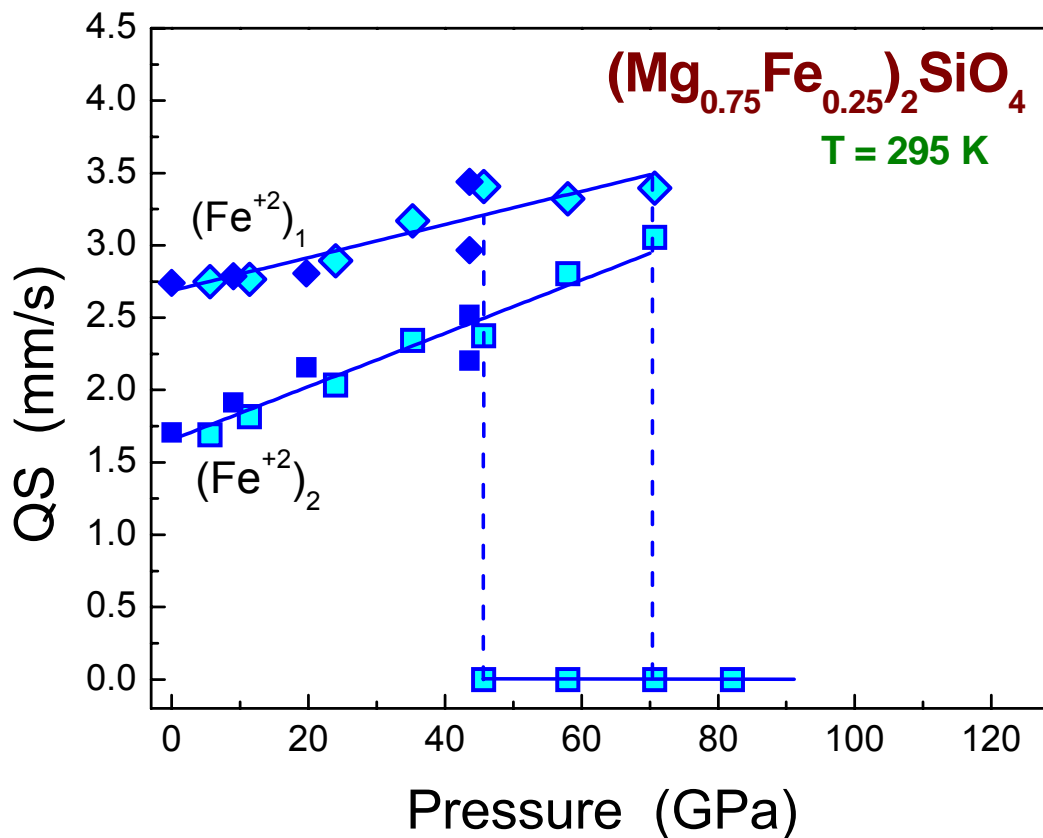Revision 2

602

603

604

605

606

607

608

609
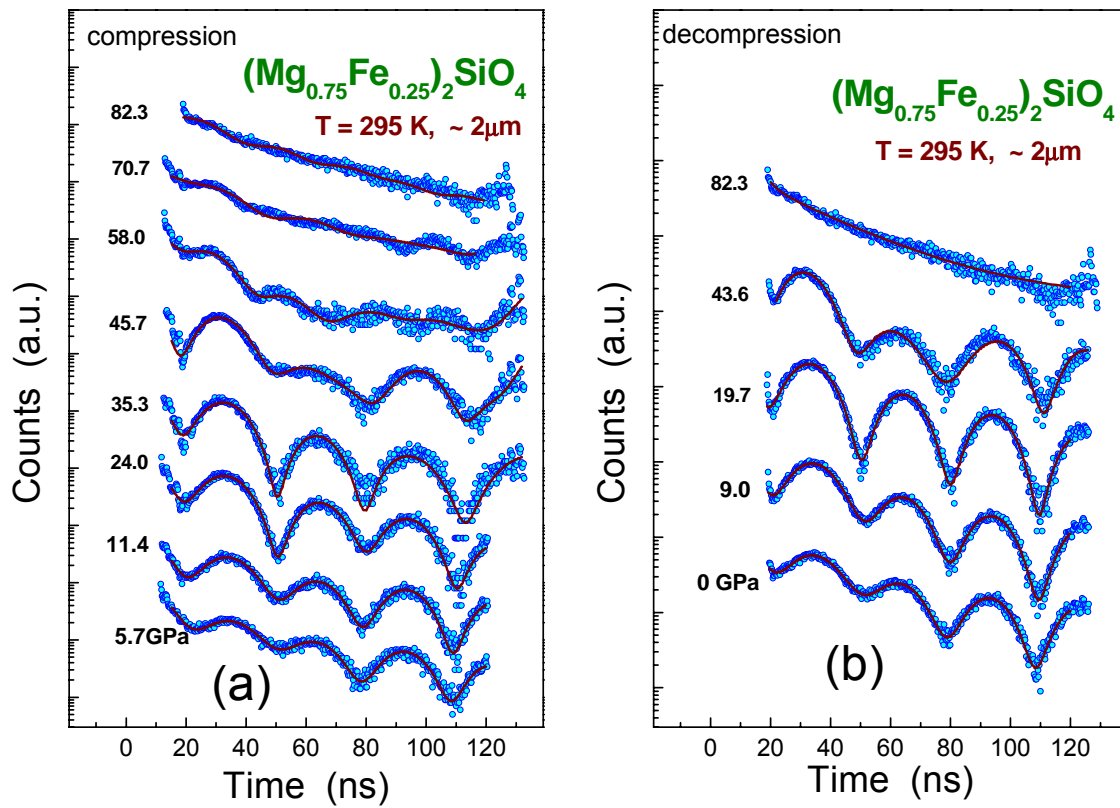
Figure 7.

Revision 2

615

616

617

618

619
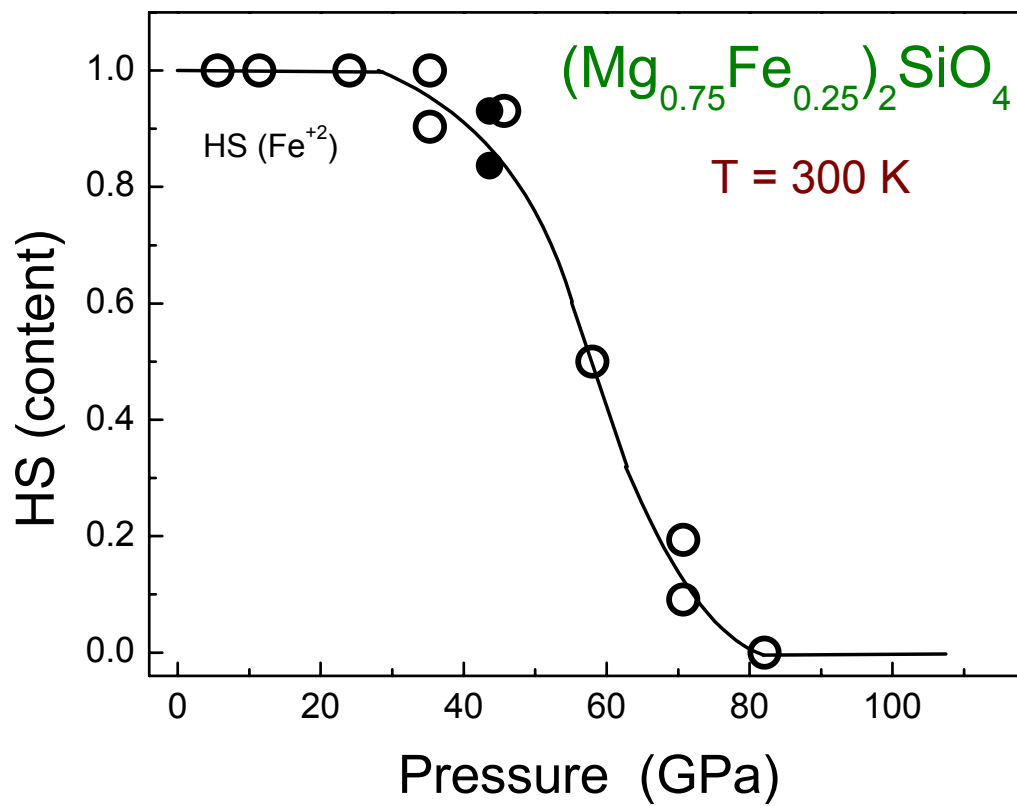

620
621

622

623

624   **Figure 8.**

625

626

627

628

629
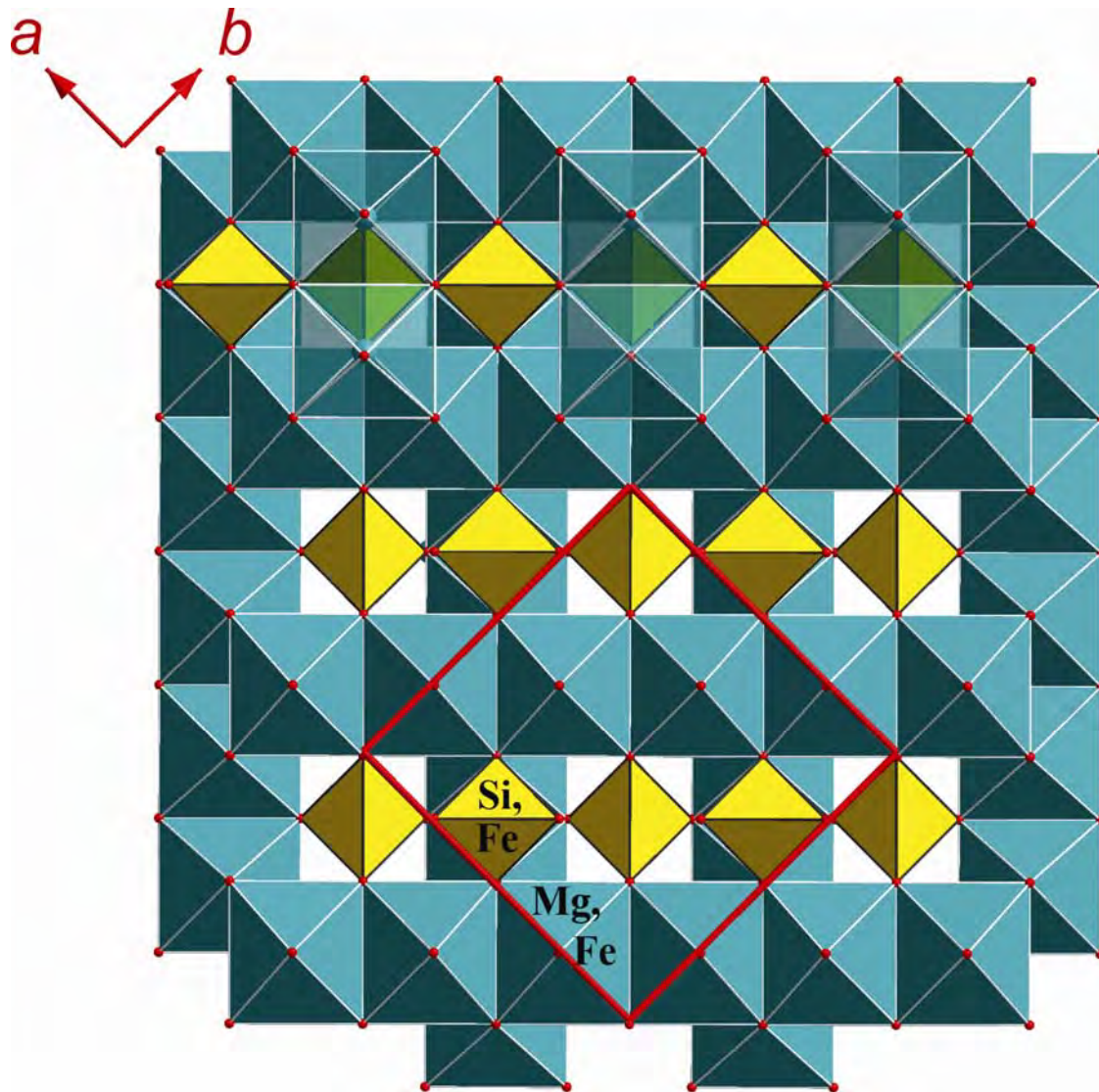

630

631

632

633 **Figure 9.**

634

Revision 2

635

636

637

638

639

640

641

642

643

Figure 10.

645